An allosteric switch regulates *Mycobacterium tuberculosis* ClpP1P2 protease function as established by cryo-EM and methyl-TROSY NMR

Siavash Vahidi[a,b,c,d,1], Zev A. Ripstein[b,d,1], Jordan B. Juravsky[d], Enrico Rennella[a,b,c,d], Alfred L. Goldberg[e], Anthony K. Mittermaier[f], John L. Rubinstein[b,d,g], and Lewis E. Kay[a,b,c,d,2]

[a]Department of Molecular Genetics, University of Toronto, Toronto, ON M5S 1A8, Canada; [b]Department of Biochemistry, University of Toronto, Toronto, ON M5S 1A8, Canada; [c]Department of Chemistry, University of Toronto, Toronto, ON M5S 1A8, Canada; [d]Program in Molecular Medicine, Hospital for Sick Children, Toronto, ON M5G 1X8, Canada; [e]Department of Cell Biology, Harvard Medical School, Boston, MA 02138; [f]Department of Chemistry, McGill University, Montreal, QC H3A 0B8, Canada; and [g]Department of Medical Biophysics, University of Toronto, Toronto, ON M5G 1L7, Canada

Edited by Michael F. Summers, University of Maryland, Baltimore County, Baltimore, MD, and approved February 3, 2020 (received for review December 9, 2019)

The 300-kDa ClpP1P2 protease from *Mycobacterium tuberculosis* collaborates with the AAA+ (ATPases associated with a variety of cellular activities) unfoldases, ClpC1 and ClpX, to degrade substrate proteins. Unlike in other bacteria, all of the components of the Clp system are essential for growth and virulence of mycobacteria, and their inhibitors show promise as antibiotics. MtClpP1P2 is unique in that it contains a pair of distinct ClpP1 and ClpP2 rings and also requires the presence of activator peptides, such as benzoyl-leucyl-leucine (Bz-LL), for function. Understanding the structural basis for this requirement has been elusive but is critical for the rational design and improvement of antituberculosis (anti-TB) therapeutics that target the Clp system. Here, we present a combined biophysical and biochemical study to explore the structure–dynamics–function relationship in MtClpP1P2. Electron cryomicroscopy (cryo-EM) structures of apo and acyldepsipeptide-bound MtClpP1P2 explain their lack of activity by showing loss of a key β-sheet in a sequence known as the handle region that is critical for the proper formation of the catalytic triad. Methyl transverse relaxation-optimized spectroscopy (TROSY)-based NMR, cryo-EM, and biochemical assays show that, on binding Bz-LL or covalent inhibitors, MtClpP1P2 undergoes a conformational change from an inactive compact state to an active extended structure that can be explained by a modified Monod–Wyman–Changeux model. Our study establishes a critical role for the handle region as an on/off switch for function and shows extensive allosteric interactions involving both intra- and interring communication that regulate MtClpP1P2 activity and that can potentially be exploited by small molecules to target *M. tuberculosis*.

protein homeostasis | allostery | intra-/interring cooperativity | ClpP handle region

Tuberculosis (TB) is an infectious disease caused by *Mycobacterium tuberculosis* that typically affects the lungs of patients (1). Without proper treatment, the mortality rate from TB is high, with ∼1.5 million deaths per 10 million new cases each year (2). TB is thus the leading cause of mortality from a single infectious agent worldwide (2). Patients with compromised immune systems, such as those treated with immunosuppressive drugs (3) or infected by HIV (4), are particularly vulnerable to infection. Drug-resistant strains of *M. tuberculosis* are increasingly common (2, 5) with 0.5 million cases of TB in 2017 resistant to rifampicin, the standard first-line drug therapeutic (2). Treatments for drug-resistant strains are complex, slow, and expensive, and they have severe side effects (6–8). Notably, it is estimated that one-quarter of the world's population is infected with latent *M. tuberculosis* (9, 10). These alarming facts emphasize the urgent need to develop novel therapeutic strategies that are effective against drug-resistant strains of *M. tuberculosis*, which in turn, requires an atomic-level understanding of the key molecular components that are responsible for maintaining the viability of this disease-causing pathogen.

The ClpP protease is a major component of one of the main protein degradation systems in many bacteria (11–14). ClpP is essential for homeostasis, pathogenesis, and virulence in several bacteria (12, 15, 16) and is considered a novel drug target for antibiotics that disrupt enzyme function as their mechanism of action (17–21). For example, cyclic acyldepsipeptides (ADEPs) cause unregulated activity in most bacterial ClpPs leading to the proteolysis of proteins necessary for survival and have proven to be an effective bactericide against antibiotic-resistant and persistent subpopulations of *Staphylococcus aureus* (22–25). In *M. tuberculosis*, ClpP1P2 (hereafter referred to as MtClpP1P2) is essential for growth and virulence (26, 27) and requires the binding of essential AAA+ (ATPases associated with a variety of cellular activities) unfoldases, ClpX or ClpC1, that use the energy of adenosine triphosphate (ATP) to unfold and translocate substrates into its

Significance

The MtClpP1P2 protease is part of the essential protein degradation machinery that helps maintain protein homeostasis in *Mycobacterium tuberculosis*, the causative agent of tuberculosis. Antibiotics that selectively kill both dormant and growing drug-resistant populations of *M. tuberculosis* by disrupting MtClpP1P2 function have attracted recent attention. Here, we characterize a switch that can control MtClpP1P2 activity through binding of small peptides, leading to a concerted conformational change that potentially can be exploited by drug molecules to interfere with MtClpP1P2 function. Overall, this work highlights the power of a combined NMR and electron cryomicroscopy approach to provide detailed insights into the structure–dynamics–function relationship of molecular machines critical to human health.

Author contributions: S.V., Z.A.R., A.L.G., J.L.R., and L.E.K. designed research; S.V., Z.A.R., J.B.J., and L.E.K. performed research; S.V., Z.A.R., J.B.J., E.R., A.K.M., and L.E.K. contributed new reagents/analytic tools; S.V., Z.A.R., A.K.M., and L.E.K. analyzed data; J.L.R. supervised the electron cryomicroscopy studies; L.E.K. supervised NMR studies; and S.V., Z.A.R., J.L.R., and L.E.K. wrote the paper.

The authors declare no competing interest.

This article is a PNAS Direct Submission.

Data deposition: The electron microscopy density maps reported in this paper have been deposited in the Electron Microscopy Databank (accession nos. EMD-21197, EMD-21198, and EMD-21199). The atomic models reported in this paper have been deposited in the Protein Data Bank (ID codes 6VGK, 6VGN, and 6VGQ). Higher-quality figures are available in Figshare (https://doi.org/10.6084/m9.figshare.11879790.v1).

See online for related content such as Commentaries.

[1]S.V. and Z.A.R. contributed equally to this work.

[2]To whom correspondence may be addressed. Email: kay@pound.med.utoronto.ca.

This article contains supporting information online at https://www.pnas.org/lookup/suppl/doi:10.1073/pnas.1921630117/-/DCSupplemental.

First published March 2, 2020.

catalytic chamber for degradation (28). Lassomycin (29), ecumicin (30), and rufomycin (31) are promising antibiotics that selectively kill both dormant and growing drug-resistant populations of *M. tuberculosis* by binding to ClpC1 and decoupling ATP-dependent protein unfolding from proteolysis. Similarly, ADEPs also kill *M. tuberculosis* by preventing the binding of AAA+ regulatory unfoldases to MtClpP1P2 (32). MtClpP1P2 reacts with standard inhibitors of serine proteases, such as chloromethyl ketones, which modify the serine and histidine residues at enzyme active sites (33). Peptide boronates have been shown to also directly engage MtClpP1P2 active sites, causing inhibition at low-micromolar concentrations and preventing growth of *M. tuberculosis* (34–36). More recently, Cediranib, an anticancer drug, was proposed as a novel noncovalent inhibitor of MtClpP1P2 (37).

Most bacteria possess a single *clpP* gene, giving rise to a structure comprising a pair of heptameric rings that are arranged coaxially to form a homotetradecameric barrel-like protein complex enclosing 14 Asp-His-Ser catalytic triads (11, 12, 38). Each of the identical protomers consists of an N-terminal domain that forms gated narrow pores on the apical surface of the barrel, a head domain that generates the main body of the ClpP barrel, and a handle region comprising a helix and a β-sheet that mediate ClpP ring–ring interactions (11, 38–40). In addition, the handle provides crucial contacts that align the catalytic triad and generates a binding groove for substrate polypeptides (41). Opening of the pores that allow substrate translocation is tightly regulated by AAA+ regulators (42, 43).

Actinobacteria, the phylum to which mycobacteria such as *M. tuberculosis* belong, are unique in that they contain two *clpP* genes, *clpP1* and *clpP2*, that encode for MtClpP1 and MtClpP2, respectively (44, 45). Initial structure–function studies concluded that MtClpP1 and MtClpP2 were separate enzymes that in isolation formed mixtures of homoheptameric and homotetradecameric complexes that lacked activity (46, 47). Later, the specific catalytically functional form of the enzyme was elucidated on the addition of small-molecule activators, such as benzoyl-leucyl-leucine (Bz-LL), that promote the formation of heterocomplexes comprising one copy of each of the MtClpP1 and MtClpP2 rings, converting the inactive enzyme to a catalytic form on binding (33). Recent studies (48) showed that mixing of MtClpP1 and MtClpP2 results in MtClpP1P2 complexes, even in the absence of activators. Unlike for other ClpPs, the addition of ADEP alone does not activate MtClpP1P2 (32, 49). The requirement for activators seems to be a unique feature of actinobacteria as other species that contain two ClpP proteoforms, such as *Listeria monocytogenes* (50, 51) and *Chlamydia trachomatis* (52), are functional even in their absence. X-ray structures of MtClpP1P2 crystalized in the presence of Bz-LL show that the overall architecture and fold of each ClpP protomer are indistinguishable from what is found in other bacterial ClpPs that retain activity in the apo form (53). Paradoxically, dipeptide activators occupy all 14 MtClpP1P2 catalytic sites in these structures, with activity arising presumably when the activators are displaced by substrate. Another crystal structure of MtClpP1P2 that includes ADEP and an Ile-Leu dipeptide activator confirms the full occupancy of peptide activator in all catalytic sites (49). In this structure, seven ADEP molecules are bound exclusively to MtClpP2 and interact with the hydrophobic pocket at the interface between two adjacent protomers. Currently, there are no structures available for the inactive apo and ADEP-bound MtClpP1P2 complexes in the absence of activators, and hence, both the structural basis for the lack of activity and the mechanism of MtClpP1P2 activation by peptides remain unclear. The lack of activity is particularly intriguing given that other ClpPs are active in the apo conformation and that their activity increases on ADEP binding.

Herein, we present a combined biophysical and biochemical study using methyl transverse relaxation optimized spectroscopy (methyl-TROSY)–based NMR (54) as well as electron cryomicroscopy (cryo-EM) to explore the structure–dynamics–function relationship in MtClpP1P2. We show that MtClpP1 and MtClpP2 exist as heptamers in solution and that on mixing they readily form MtClpP1P2 tetradecamers, even in the absence of activators. NMR titration data quantify the interaction between MtClpP1 and MtClpP2, establishing that binding becomes stronger in the presence of the Bz-LL–activating dipeptide. Structures of the inactive apo-MtClpP1P2 and ADEP-bound MtClpP1P2 complexes determined by cryo-EM explain their lack of activity by revealing the absence of a key β-sheet in the handle region that is present in all active ClpP conformations. Methyl-TROSY–based spectra show that, on binding Bz-LL, a significant conformational change occurs for MtClpP1P2 that corresponds to a conversion from an inactive state to an active structure. The NMR-based Bz-LL titration data and extensive activity profiles as a function of both Bz-LL and substrate concentrations can be explained by a modified Monod–Wyman–Changeux (MWC) model that highlights the extensive allostery in this system. Our study establishes a critical role for the handle region, serving as an on/off switch for function, and a strong network of allosteric interactions involving both intra- and interring communications that regulate activity of the MtClpP1P2 enzyme.

Results

Probing the Oligomeric State of MtClpP1P2. MtClpP1 and MtClpP2, lacking their propeptide sequences as established from previous work (33, 48), were overexpressed in *Escherichia coli* and purified as detailed in *SI Appendix*. Size exclusion chromatography (SEC) was used to probe the oligomeric forms of MtClpP1 and MtClpP2 in isolation and when mixed. MtClpP1 (residues 7 to 200) elutes at the same retention volume as a separately isolated R171A mutant of ClpP from *S. aureus* (SaClpP) that is known to form a heptameric single ring (23) (0.5 mL injected at 175 μM monomer) (Fig. 1*A*, green trace; black arrow in Fig. 1*A* denotes the elution position of R171A SaClpP). Increasing or decreasing the injected protein concentration threefold from 175 μM monomer to 525 or 58 μM, respectively, does not change the SEC peak elution volume and profile (*SI Appendix*, Fig. S1*A*), suggesting that the single ring is stable. SEC of the mature form of MtClpP2 with native propeptide processing that removed the N-terminal 12 residues (residues 13 to 214) revealed a pair of peaks at retention volumes of 11 and 13 mL that correspond to assemblies, which are either larger or approximately the same size as tetradecameric wild-type (WT) SaClpP, respectively (0.5 mL injected at 100 μM monomer) (*SI Appendix*, Fig. S1*B*, blue trace). Unfortunately, this construct is aggregation prone and polydisperse. Inspired by previous work (48), an MtClpP2 construct with three additional residues removed from the N terminus, Δ15 MtClpP2 (16 to 214), was used in the present study (*SI Appendix*, Fig. S1*C*); Δ15 MtClpP2 exhibits indistinguishable peptidase activity in MtClpP1P2 complexes relative to the original MtClpP2 protein (*SI Appendix*, Fig. S1*D*), and millimolar concentration solutions are stable for at least several weeks at 4 °C. SEC analysis of Δ15 MtClpP2 (hereafter referred to as MtClpP2) showed a purely heptameric form that elutes at the same volume as MtClpP1 (0.5 mL injected at 175 μM) (Fig. 1*A*, blue trace), and its oligomeric distribution is similarly insensitive to protein concentration (*SI Appendix*, Fig. S1*C*). Mixing of MtClpP1 and MtClpP2 yields a larger oligomeric species, corresponding to an MtClpP1P2 complex (0.5 mL injected at 175 μM of each of MtClpP1 and MtClpP2) (Fig. 1*A*, purple trace) that elutes at the same volume as the well-characterized tetradecameric SaClpP (Fig. 1*A*, black trace). Notably, the original (13 to 214) MtClpP2 construct was also able to bind MtClpP1 (*SI Appendix*, Fig. S1*B*, purple trace).

Characterization of the Interaction between MtClpP1 and MtClpP2. Peptidase assays were performed to functionally characterize MtClpP1P2 by monitoring the fluorescence change resulting from cleavage of the fluorogenic substrate peptide *N*-acetyl-Pro-Lys-Met-7-amino-4-methylcoumarin (PKM-AMC) (36). Notably, neither

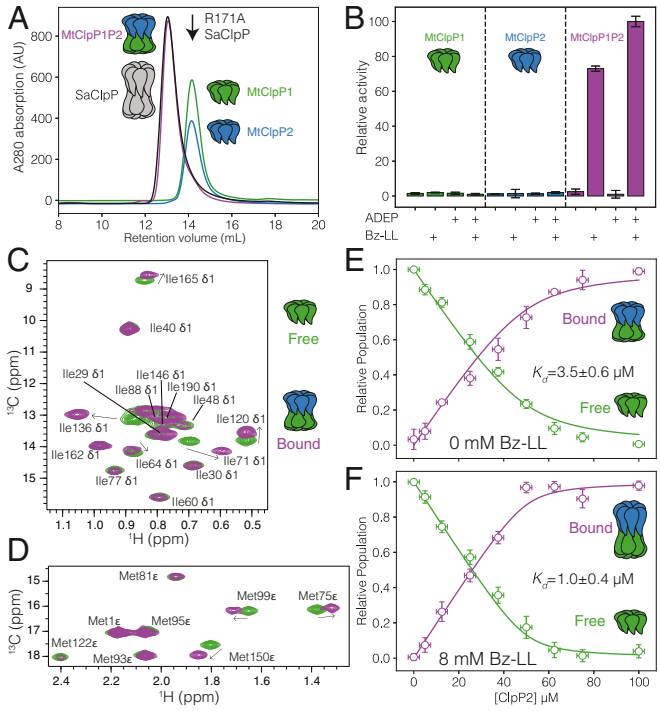

Fig. 1. Characterization of the interaction between MtClpP1 and MtClpP2. (*A*) SEC profiles of isolated MtClpP1 (residues 7 to 200; green trace) and MtClpP2 (residues 16 to 214; blue trace) and a mixture containing equimolar amounts of the two (purple trace). The SEC elution profile of WT tetradecameric SaClpP (black trace) and the elution volume of an R171A, heptameric mutant of SaClpP (black arrow) are included. In all cases, 0.5 mL of protein at a concentration of 175 μM (monomer) was injected. A280 = absorbance at 280 nm. (*B*) Peptidase activity assays, 40 °C, on isolated MtClpP1 (green bars) and MtClpP2 (blue bars) and mixtures containing equimolar amounts of the two (purple bars) performed in the presence or absence of Bz-LL (4 mM) and/or ADEP (25 μM) activators with 250 μM PKM-AMC used as substrate. In all cases, the concentration of each of MtClpP1 and MtClpP2 was 1 μM (monomer concentration). Error bars correspond to one SD based on three measurements. (*C* and *D*) Overlay of the (*C*) Ile and (*D*) Met regions of ^{1}H-^{13}C HMQC correlation maps of ILVM-labeled MtClpP1 (green contour) and a mixture containing 50 μM ILVM-labeled MtClpP1 and 100 μM [U-^{2}H] MtClpP2 (purple contours) recorded at 40 °C, 18.8 T, with assignments. (*E* and *F*) Changes in the intensity of the apo (green circles) and bound peaks (purple circles) in a titration of [U-^{2}H] MtClpP2 into 50 μM ILVM-labeled MtClpP1 in the (*E*) absence or (*F*) presence of 8 mM Bz-LL. Error bars correspond to one SD measured across all peaks averaged (vertical) or uncertainties in protein concentrations based on repeat concentration measurements (horizontal), and the solid lines are fits to a simple binding model (*SI Appendix*). The fitted dissociation constant plus or minus twice the SD is indicated in each plot.

MtClpP1 nor MtClpP2 in isolation was active (Fig. 1*B*, green and blue), with MtClpP1, MtClpP2, and Bz-LL all required for activity (Fig. 1*B*, second purple bar). The addition of ADEP to this mixture results in further activation (Fig. 1*B*, fourth purple bar). Unlike ClpPs from other organisms, MtClpP1P2 is not activated by ADEP alone (Fig. 1*B*, third purple bar). These assays establish that the MtClpP1 and MtClpP2 constructs used in this work have similar functional properties as those found in previous reports (33, 48, 49, 53).

In order to characterize the binding between MtClpP1 and MtClpP2 more quantitatively, we used methyl-TROSY NMR spectroscopy that exploits dipolar cross-correlated spin relaxation to significantly improve spectral sensitivity and resolution in high-molecular weight protein complexes (54–56). This approach is optimal in concert with selective isotopic labeling of methyl groups ($^{13}CH_3$), such as those of Ile (I), Leu (L), Val (V), and Met (M), within an otherwise uniformly deuterated ([U-^{2}H]) protein, where the prochiral methyls of Leu/Val are $^{13}CH_3/^{12}CD_3$ (referred to hereafter as ILVM labeling) (57). Here, ^{1}H-^{13}C heteronuclear multiple-quantum coherence (HMQC) correlation maps are recorded that benefit from this methyl-TROSY effect (54). High-quality spectra were obtained for samples of isolated ILVM-labeled MtClpP1 rings and when perdeuterated, and hence, NMR-invisible MtClpP2 is added to form an MtClpP1P2 complex (Fig. 1*C*). Notably, spectral quality for the MtClpP1 heptamer is superior to that for the corresponding MtClpP2 ring, and for this reason, we focused on molecules where MtClpP1 was labeled. Resonance assignments of MtClpP1 ILVM methyl probes were obtained through a combined approach involving single-point mutagenesis and analysis of nuclear Overhauser effect datasets aided by the availability of high-resolution X-ray crystal structures of MtClpP1 (46, 53). The Ile (Fig. 1*C*, green contours) and Met (Fig. 1*D*, green contours) regions of a two-dimensional (2D) ^{1}H-^{13}C HMQC spectrum of ILVM-labeled MtClpP1 recorded at 40 °C and 18.8 T have been completely assigned (17 Ile and 8 Met residues). Corresponding spectral regions and stereospecific assignments for all 7 Val and 14 of 18 Leu methyl residues are shown in *SI Appendix* (*SI Appendix*, Fig. S2, green contours). The addition of [U-^{2}H] MtClpP2 leads to the emergence of separate peaks for residues proximal to the ring–ring interface or associated with the handle region (e.g., Ile71, Ile120, Ile165, Val145, Met75, Met99, and Met150) (Fig. 1 *C* and *D* and *SI Appendix*, Fig. S2 *A*, purple contours and *B*). These new peaks report the binding of MtClpP1 and MtClpP2 to form the MtClpP1P2 tetradecameric complex, and the observation of separate resonances for the apo (MtClpP1) and bound (MtClpP1P2) states establishes that their interconversion is slow on the NMR chemical shift timescale. An NMR titration was performed to obtain binding constants for the MtClpP1 and MtClpP2 interaction (Fig. 1*E*). For residues with well-resolved peak displacements on binding of MtClpP2, intensities of apo (Fig. 1*E*, green) and bound peaks (Fig. 1*E*, purple) were averaged and fitted with a simple binding model (*SI Appendix*). This analysis, which includes errors in peak intensities (y axis) and in protein concentration (x axis), yielded a dissociation constant of 3.5 ± 0.6 μM in the absence of Bz-LL activator. The interaction between MtClpP1 and MtClpP2 is moderately strengthened in the presence of 8 mM Bz-LL, with a dissociation constant of 1.0 ± 0.4 μM (*SI Appendix*, Fig. S2*C*).

Cryo-EM Structure of Apo MtClpP1P2 Explains Its Lack of Activity. Several crystal structures of MtClpP1P2 bound to dipeptide activators have been reported showing that the complex adopts the active extended conformation (53), similar to the structures of other ClpPs that are functional without the addition of activating molecules (38, 39, 58, 59). The absence of a high-resolution structure for apo-MtClpP1P2 has precluded an understanding of the underlying reason for the lack of activity for *M. tuberculosis* ClpP. To address this question, MtClpP1 and MtClpP2 heptamers were mixed, and the resulting apo MtClpP1P2 complex was isolated using SEC and subjected to cryo-EM analysis. Following 2D classification (*SI Appendix*, Fig. S3 *A* and *B*), 373,064 particle images were used for a final refinement with C7 symmetry, achieving a resolution of 3.1 Å (*SI Appendix*, Fig. S4 *A* and *B*). Further classification without enforcing symmetry did not yield additional conformations. The refined map shows a tetradecameric arrangement, comprising a pair of heptameric MtClpP1 and MtClpP2 rings (Fig. 2*A*), akin to the Bz-LL–bound MtClpP1P2 structure that was solved to 3.0 Å by X-ray crystallography (53) (Fig. 2*B*) (Protein Data Bank [PDB] ID code 5DZK) and subsequently confirmed in the present study. Whereas the Bz-LL–bound structure is in the active extended conformation, the apo form appears to adopt the "compact" state characterized by a shorter barrel height (83 vs. 87 Å) (Fig. 2 *A* and *B*). Compression of the barrel is accompanied by disruption

of the handle β-sheet (Fig. 2 *C* and *D*), which in the active conformation, connects pairs of protomers from opposite rings. In the apo structure, the two strands move apart and become more flexible as suggested by lower resolution for these strands relative to the rest of the protein complex (Fig. 2*E* and *SI Appendix*, Figs. S5*A* and S6). This disorder/flexibility is particularly notable for MtClpP2. Flexibility in the handle region is also supported by our NMR data, where a comparison of MtClpP1 methyl peak intensities in a spectrum of the MtClpP1P2 complex shows that the most intense correlations derive from the γ1 and γ2 methyl groups of the handle residue V129 and the δ1 methyl from I162, a residue that packs against the handle region. Indeed, an analysis of relative peak intensities suggests that many of the handle residues have above-average dynamics. The handle region is critically important for function as it positions the catalytic triad for optimal activity and provides a binding groove for ClpP substrates (Fig. 2 *C* and *D*). In both MtClpP1 and MtClpP2 rings, the catalytic His residue (His123 in MtClpP1) is located three amino acids N-terminal to the start of the handle β-sheet. The disordered conformation of the handle region displaces His123 from its position in the active conformation, thereby preventing the proper orientation of the catalytic triad residues (Fig. 2 *F* and *G*). A well-known requirement of ClpP activity is engagement of oligomeric sensors comprising a pair of Asp-Arg salt bridges that link protomers in opposite rings and couple oligomerization with catalysis by stabilizing the active extended conformation (23, 50, 60). In contrast to the case in the apo-MtClpP1P2 structure where the oligomeric sensors are disengaged (Fig. 2*H*), in the Bz-LL–bound structure all

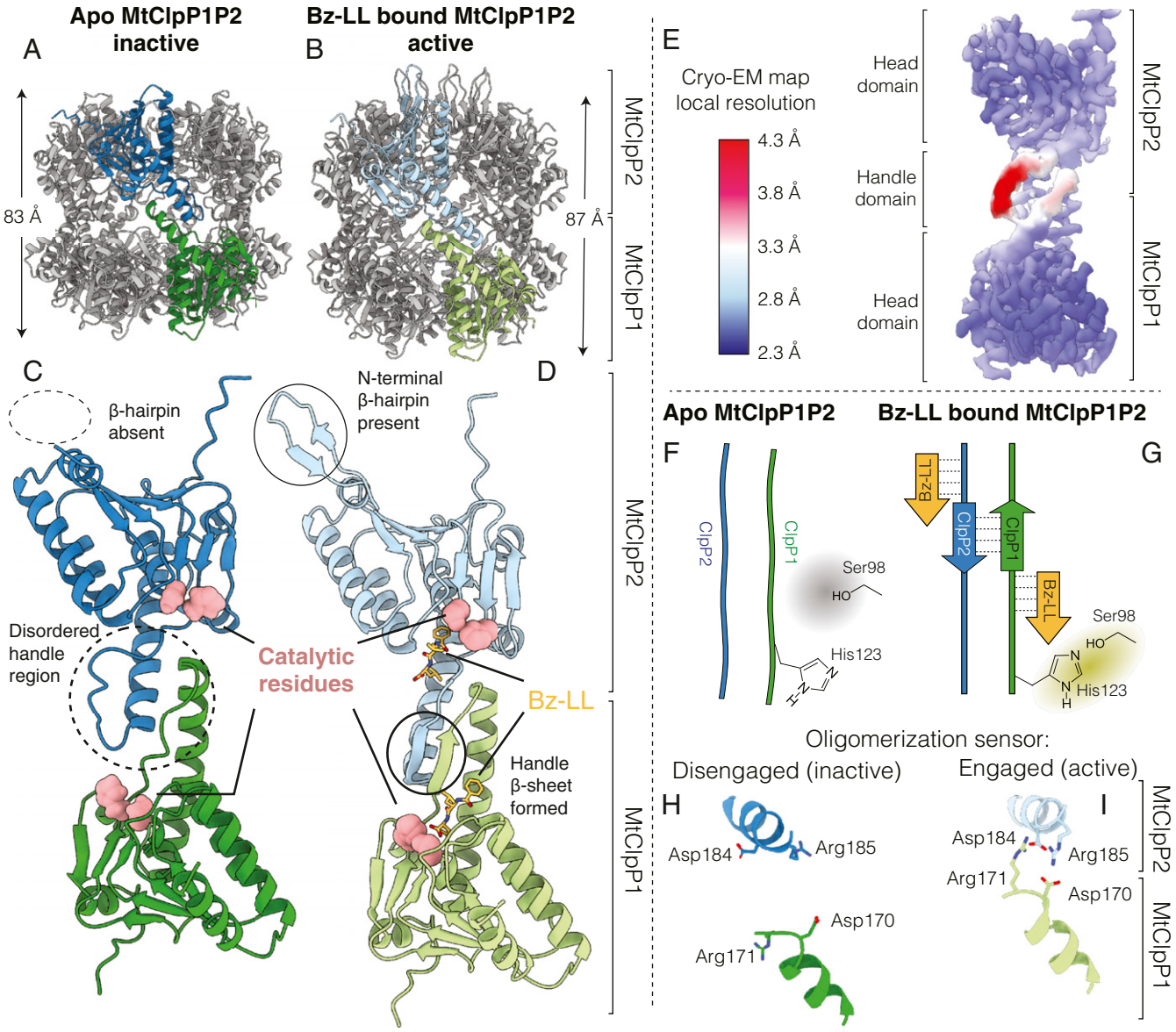

Fig. 2. Structural basis for the lack of activity of apo MtClpP1P2. (*A* and *C*) Cryo-EM structure of apo MtClpP1P2 (this study) and (*B* and *D*) crystal structure of Bz-LL–bound MtClpP1P2 obtained from ref. 53 (PDB ID code 5DZK). In each case, a pair of MtClpP1 (green) and MtClpP2 (blue) protomers is colored to show the ring–ring interaction interface. The height of the ClpP barrel (excluding the N-terminal β-hairpins of MtClpP2) is denoted in each case. Major structural differences between apo and Bz-LL–bound MtClpP1P2 are highlighted. (*E*) Cryo-EM density map of apo MtClpP1P2 at 3.1-Å resolution refined using C7 symmetry, with the distribution of local resolution color coded as indicated. (*F* and *G*) Schematic showing how the conformation of the handle β-sheets is affected by Bz-LL binding and its influence on positioning of the catalytic His. (*H* and *I*) Status of the oligomerization sensor in the apo and Bz-LL–bound forms of MtClpP1P2. Side chains of residues involved in salt bridge formation are indicated.

seven Asp170-Arg171 salt bridges connecting opposite rings are observed (Fig. 2*I*).

Structural Basis for Inactivity of ADEP-Bound MtClpP12. The assays shown in Fig. 1*B* establish that apo-ClpP1P2 is not catalytically active, with the structural basis for this lack of activity explained by the model of the apo-MtClpP1P2 complex showing a disordered handle region. Given that binding of a variety of different ADEPs fails to activate MtClpP1P2, including ADEP-7 assayed here as well as six different analogs studied elsewhere (49), we postulated that this class of activator would not be able to reorganize the handle into a catalytically competent form. In order to test this hypothesis, we calculated a 3.1-Å-resolution cryo-EM map of MtClpP1P2 bound to ADEP (*SI Appendix*, Fig. S4 *C* and *D*). After 2D classification, 192,430 particle images were used in a final refinement step with C7 symmetry enforced (*SI Appendix*, Fig. S3 *C* and *D*). Further classification without enforcing symmetry did not reveal additional conformations. As in the apo structure, the height of the barrel is 83 Å (excluding N-terminal gates) (Fig. 3*A*). There is clear density for seven ADEP molecules at the interface of the MtClpP2 protomers (Fig. 3 *A*, *Inset*), with no ADEP bound to MtClpP1 (Fig. 3 *B* and *C*), consistent with biochemical evidence (48) and published crystal structures of MtClpP1P2 bound to both ADEP and dipeptide activator (49). Compared with apo-MtClpP1P2, ADEP binding causes a striking rigidification of the MtClpP2 N-terminal β-hairpins (Fig. 3*C*). Importantly, the handle region remains disordered (Fig. 3*C* and *SI Appendix*, Fig. S5*B*), and the oligomeric sensor is disengaged (Fig. 3*D*). Apart from the conformational changes that ADEP binding introduces to MtClpP2, the overall fold and conformation of MtClpP1 resemble those of the apo form, with an rmsd between MtClpP1 rings of only 0.29 Å (Fig. 3*B*). Interestingly, activity response curves using PKM-AMC as substrate, for which only MtClpP1 has significant activity (*SI Appendix*, Fig. S7), show a shift to lower Bz-LL values on the addition of ADEP (Fig. 3*E*). This observation is consistent with an interring allosteric communication originating from the ADEP binding site on the apical surface of MtClpP2 that propagates to the active sites of MtClpP1.

An Allosteric Framework for Understanding MtClpP1P2 Activation and Function. The results of the previous section show that binding of ADEP to MtClpP2 leads to a shift in the activity

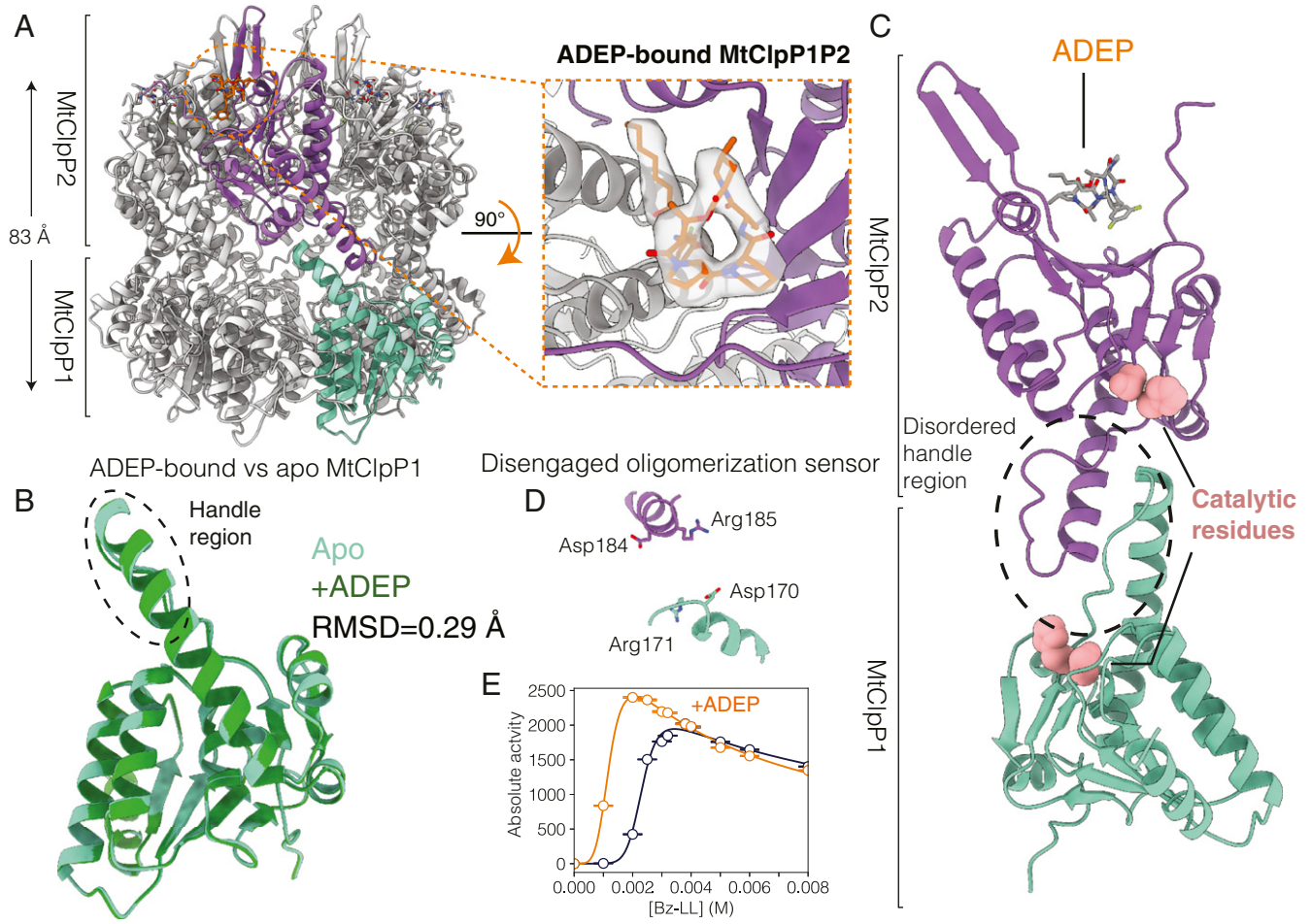

Fig. 3. Structural basis for the lack of activity of ADEP-bound MtClpP1P2. (*A*) Side view of a cryo-EM structure of MtClpP1P2 bound to ADEP only. The height of the MtClpP1P2 barrel (excluding the N-terminal β-hairpins of MtClpP2) is denoted. *Inset* shows the top view of the MtClpP1P2 complex looking down into the ADEP binding pocket at the interface of a pair of adjacent MtClpP2 protomers. The cryo-EM density corresponding to bound ADEP is displayed. (*B*) The rmsd and overlay of single MtClpP1 protomers from MtClpP1P2 structures in the apo (light green) and the ADEP-bound (dark green) forms. Notably, the handle region (circled) remains disordered in the ADEP-bound form as in the apo structure. (*C*) Magnified view of a pair of opposite MtClpP1 (cyan) and MtClpP2 (purple) protomers shown to highlight the disordered handle region and its position relative to the catalytic residues and the bound ADEP molecule. (*D*) Status of the oligomerization sensor in the ADEP-bound MtClpP1P2 complex. The side chains of residues involved in salt bridge formation in the active Bz-LL–bound conformation are indicated. (*E*) Activity response curves, 40 °C, measured as a function of Bz-LL concentration using 250 μM PKM-AMC as substrate in the absence (blue curve) and presence (orange curve) of 25 μM ADEP.

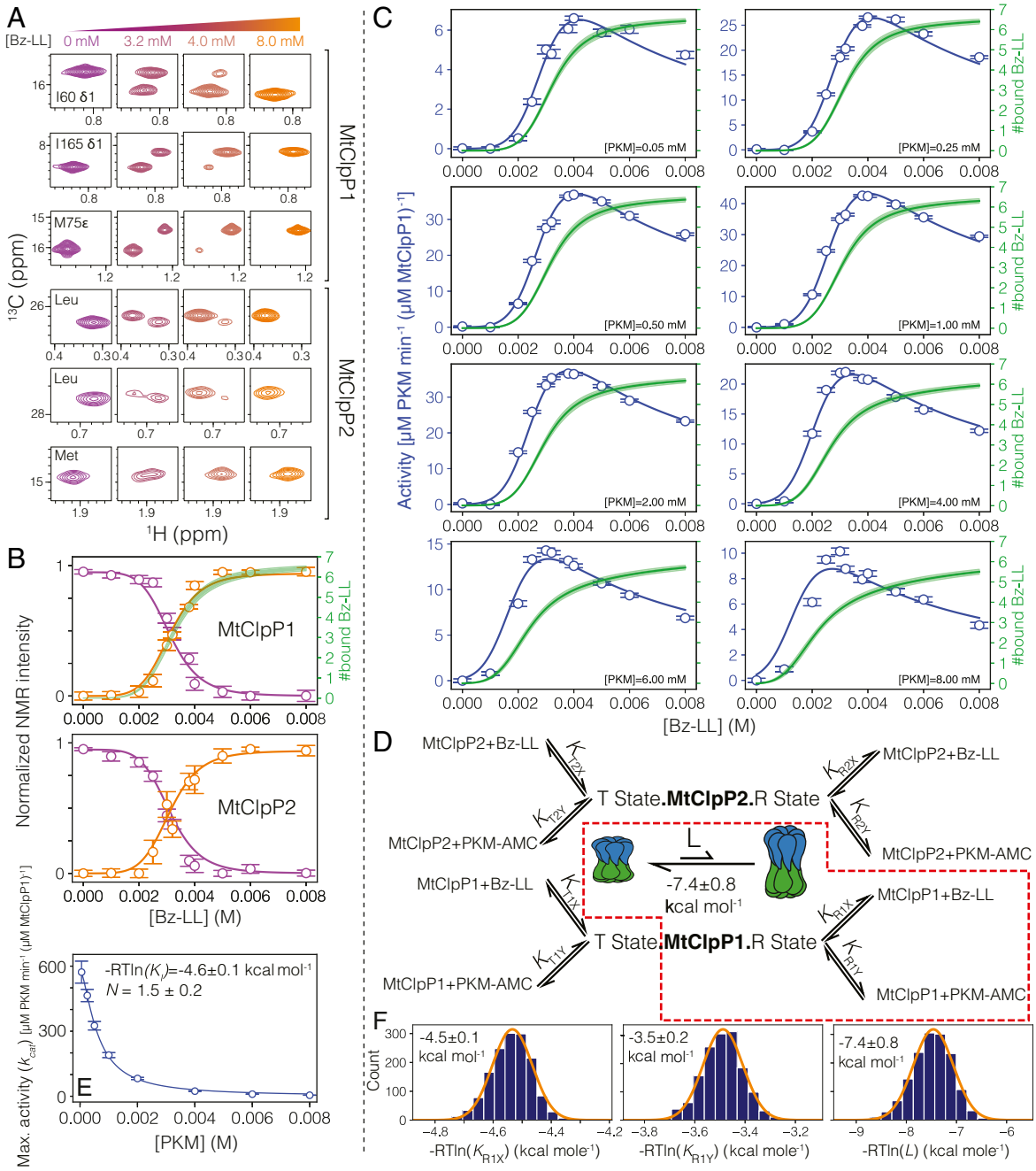

Fig. 4. An allosteric network regulates the activation of MtClpP1P2. (*A*) Changes in correlations in ^{1}H-^{13}C HMQC spectra of MtClpP1P2 recorded as a function of Bz-LL concentration, 40 °C, 18.8 T, reflect interconversion between conformers on a slow timescale. The first three rows show spectral regions of datasets recorded on an MtClpP1P2 complex where MtClpP1 is ILVM labeled (50 μM), while MtClpP2 is [U-^{2}H] (100 μM). Assignments for MtClpP1 residues are indicated. The labeling pattern and protein concentrations are reversed in spectra of the bottom three rows. Assignments for MtClpP2 are not available, and therefore, only residue types are noted. (*B*) Changes in the intensities of *T*-state (purple circles) and *R*-state (orange circles) peaks averaged for resonances from MtClpP1 and MtClpP2 of the MtClpP1P2 complex. Error bars correspond to one SD based on all peaks averaged. Solid lines are fits to *SI Appendix*, Eqs. **S11** and **S12** using a simplified version of the modified MWC model, whereby only the region highlighted by the dashed red box in *D* is included in the analysis (i.e., all equilibrium constants are set to zero with the exception of K_{R1X} and K_{R1Y}). Note that profiles in *B* and *C* were fit simultaneously. The number of Bz-LL molecules bound to MtClpP1 rings (green line; thickness indicates an error of two SDs from the mean) is calculated by evaluating *SI Appendix*, Eq. **S17** using the fitted K_{R1X} and K_{R1Y} values. (*C*) Activity of MtClpP1P2 measured at various Bz-LL and PKM-AMC concentrations (blue circles) and best fits of the data to *SI Appendix*, Eq. **S13** (blue lines) (*SI Appendix*) using a simplified version of the modified MWC model (red box in *D*). In each panel, curves (solid green; ±2 SD from the mean) showing the number of Bz-LL molecules bound to the *R* state of MtClpP1 are calculated from *SI Appendix*, Eq. **S17** as above. (*D*) Schematic representation of the derived MWC model along with the simplified model used for global fitting of the NMR and functional data in this figure (red dashed box) (*SI Appendix*, Fig. S8 shows the fitting of the complete model), including the $T \rightleftharpoons R$ equilibrium, with equilibrium constant $L = \frac{[T]}{[R]}$. The relevant association constants are indicated in gray. (*E*) The decrease in k_{cat} $[V_o([Y])]$ (*SI Appendix*, Eq. **S13**) as a function of substrate PKM-AMC concentration (open circles) fitted to a Hill-type substrate inhibition model (solid line). The fitted association constant ($-$RTlnK_i) for substrate binding to a distinct inhibitory site and the Hill constant (N) are listed. Errors are based on a Monte Carlo analysis discussed in *SI Appendix*. (*F*) The fitted free energies for Bz-LL and PKM-AMC binding to the *R* state of the MtClpP1 ring are listed, 40 °C, along with the distribution of values based on a Monte Carlo analysis. The distributions in *F* are fitted to a Gaussian function, and the errors are reported as twice the SD in the parameters.

profile of MtClpP1 that is most readily understood in the framework of an allosteric system. We next sought to address whether the binding of Bz-LL to the MtClpP1P2 complex was similarly allosteric. Initial NMR titrations made use of samples prepared with ILVM-labeled MtClpP1 (50 μM in protomer concentration) and a twofold excess of [U-^{2}H] MtClpP2, ensuring that more than 90% of the NMR-visible MtClpP1 ring forms a complex. Addition of Bz-LL leads to residue-specific titration profiles in which peaks present in the absence of ligand decrease in intensity concomitant with the appearance of new resonances as would be expected for a system in slow exchange on the NMR chemical shift timescale (Fig. 4*A*, rows 1 to 3). Notably, nearly all of the ILVM methyl probes within the MtClpP1 ring respond to the addition of Bz-LL in this manner. A similar situation is observed for resonances derived from MtClpP2 when samples are prepared by reversing the labeling strategy indicated above (Fig. 4*A*, rows 4 to 6), and the titration profiles for MtClpP1 and MtClpP2 are essentially superimposable (described below). Because the spectrum of MtClpP2 is of relatively poor quality, we did not attempt to assign individual correlations to specific sites in the protein, and therefore, assignments for the selected residues in this ring are not available. Notably, the observed chemical shift changes were confined to the MtClpP1P2 complex; no changes to spectra of either isolated MtClpP1 or MtClp2 were observed when comparable amounts of Bz-LL were added, suggesting that the spectral perturbations report on a conformational change that only occurs in the full complex.

The decrease in the intensities of apo peaks (purple correlations in Fig. 4*A*, 0 mM) along with the concomitant increase in the intensities of the new set of correlations (orange correlations in Fig. 4*A*, 8 mM) is quantified in Fig. 4*B* for resonances from both MtClpP1 and MtClpP2 of the MtClpP1P2 complex. Here, we have averaged the corresponding curves from each methyl probe (52 and 51 peaks from MtClpP1 and MtClpP2, respectively). When the averaged MtClpP1 and MtClpP2 profiles are fit separately to the simple Hill model for cooperative binding (solid lines in Fig. 4*B*), effective dissociation constants of 3.3 ± 0.2 mM (MtClpP1) and 3.1 ± 0.2 mM (MtClpP2) are obtained along with Hill coefficients of 7.4 ± 0.9 and 7.9 ± 0.7, respectively, in each case, indicative of a highly cooperative transition.

The millimolar K_d values that have been fitted here are typically associated with binding events where the exchange kinetics are fast on the NMR chemical shift timescale. In this limit, peak positions are shifted in a manner that reflects the relative populations of apo and bound conformers without an increase in the number of peaks during the course of the titration that was observed here. In the present case, an upper bound of 1 to 2 s^{-1} can be placed on the exchange rate between the observed pair of conformers based on the fact that exchange cross-peaks were not obtained in magnetization exchange experiments (61). Our results suggest, therefore, that the observed chemical shift behavior does not correspond to a simple binding process. Indeed, separate titration profiles are obtained for a number of peaks that do shift in position as a function of [Bz-LL] as would be observed for a fast-exchange, low-affinity case. Unfortunately, we are not able to quantify these shifts properly to obtain a measure for the Bz-LL affinity because the shifts do not reach a plateau value at the concentrations used, and the changes in shift are small.

The slow exchange process that is seen on addition of Bz-LL (Fig. 4 *A* and *B*), and which we have quantified here most likely reflects a conformational change in the MtClpP1P2 complex that ensues on Bz-LL binding, likely from the inactive, compact state that is observed in our cryo-EM–derived structures (Fig. 2 *A* and *C*) to the active, extended form that has been characterized by crystallography (53) (Fig. 2 *B* and *D*). Functional assays performed over a range of PKM-AMC substrate concentrations are consistent with this interpretation (Fig. 4*C*, open circles). In these assays, MtClpP1P2 is inactive in the absence of Bz-LL as expected since the handle region is not properly formed without activator (Fig. 2*C*). At ∼2.5 mM Bz-LL, MtClpP1P2 activity begins to increase sigmoidally until it reaches a maximum at ∼4 mM Bz-LL followed by inhibition at higher Bz-LL concentrations (Fig. 4*C*). Notably, the rise in activity (Fig. 4*C*, blue circles) parallels the transition observed for both MtClpP1 and MtClpP2 as reported by the changes in peak intensities in NMR spectra (Fig. 4*B*, orange circles). There is thus a strong link between the NMR observations (Fig. 4*B*), the functional assays (Fig. 4*C*), and the structural changes characterized by cryo-EM (Fig. 2*C*).

To gain a quantitative understanding of MtClpP1P2 activation by Bz-LL, we sought to simultaneously fit the NMR titration data (Fig. 4*B*, open circles) and the functional assays (Fig. 4*C*, open circles) to an allosteric binding model. One of the simplest and most intuitive models is that due to Monod, Wyman, and Changeux, termed the MWC model (62), and we have used a modified version that incorporates specific features of the MtClpP1P2 complex (Fig. 4*D*; *SI Appendix* has the derivation of the model). As in the original derivation, we assume that each of the protomers of a given type, such as those from, for example, MtClpP1, is equivalent and that binding of substrate or activator at one site does not change the microscopic constants for binding at other locations. In addition as described previously (62), all protomers can exist in one of two states termed *T* (low activity) or *R* (high activity), with all seven protomers in a given ClpP ring in the same *R* or *T* conformation. A number of further assumptions are necessary. 1) As our Bz-LL titration data clearly establish that a conformational transition occurs simultaneously for both MtClpP1 and MtClpP2 (compare *Upper* and *Lower* in Fig. 4*B*), it is assumed that all protomers in both ClpP rings are in same conformation, either *T* or *R*. MtClpP1P2 tetradecamers where one of the ClpP rings is entirely *R* and the second is entirely *T* are, therefore, not allowed. 2) Activity assays where the MtClpP1 ring is inactivated by mutation of the catalytic Ser in each of its seven protomers, MtClpP1(S98A)P2, show that maximum PKM-AMC hydrolysis rates are over 10-fold lower than for WT MtClpP1P2 (*SI Appendix*, Fig. S7). We assume, therefore, that enzyme activity is solely governed by the number of substrate molecules bound to MtClpP1 that, in turn, is only active (capable of proteolysis) in the *R* state. 3) Sites in MtClpP1 or MtClpP2 bind substrate and activator in a competitive manner so that only one molecule of either substrate or activator is bound to a given site at a time. With these assumptions, a set of equations can be derived that includes eight microscopic binding constants for the association of either substrate (PKM-AMC) or activator (Bz-LL) to protomers from either MtClpP1 or MtClpP2 rings that, in turn, are either both in *R* or both in *T* states (for example, K_{R1X} is the microscopic association constant for binding of Bz-LL to each of the seven protomers of the MtClpP1 ring of an MtClpP1P2 complex that is in the *R* state) (Fig. 4*D*). In addition, an equilibrium constant $L = \frac{[T]}{[R]}$ is required in the fits, where [*T*] and [*R*] are the concentrations of MtClpP1P2 in the *T* and *R* states in the absence of Bz-LL, respectively, as well as a k_{cat} value that "converts" the average number of substrate molecules bound to the *R* state of the MtClpP1 ring to the measured substrate hydrolysis rates (i.e., enzyme activity).

Global fitting of the NMR titration data (four curves; two for each of MtClpP1 and MtClpP2 rings) (Fig. 4*B*) together with the functional assays at 8 PKM-AMC and 11 Bz-LL concentrations (Fig. 4*C*) to a set of equations presented in *SI Appendix* produced poor fits of the data, especially for higher concentrations of PKM-AMC, where rates were predicted to be significantly larger than those observed. Next, we attempted to fit all of the activity profiles with a shared set of ligand association constants as before but using distinct k_{cat} values for each substrate concentration. Notably, in this case, excellent fits were obtained, and

interestingly, the k_{cat} values so generated were reasonably well fit to a Hill curve, $Maximum\ Activity = V_{max}(1 + K_I^N[PKM]^N)^{-1}$ (*SI Appendix*), that takes into account the decrease in maximum subunit activity [i.e., k_{cat} or $V_o([Y])$ of *SI Appendix*, Eq. **S13**] with substrate concentration (substrate inhibition; discussed below). Values of $N = 1.5 \pm 0.2$ and $K_I = 1.6 \pm 0.3 \times 10^3$ M^{-1} were obtained, where K_I is the association constant for the binding of one molecule of PKM-AMC to a distinct inhibitory site in each protomer (Fig. 4*E*). Although this model yielded excellent fits of the experimental data over the complete range of substrate and activator concentrations used (*SI Appendix*, Fig. S8), the majority of the parameters could not be obtained in a robust manner due to significant cross-talk between them, leading to large uncertainties in fitted values. We, therefore, sought a simpler version of the more general scheme of Fig. 4*D* that would capture the behavior of the system, with a smaller number of fitted parameters that could be extracted more robustly from the data. The simplest scheme that could fit the data is highlighted by the red box in Fig. 4*D*, where only a single ring is considered corresponding to MtClpP1. It might be expected that a single MtClpP1 ring would be a good starting point for describing the activity profile since MtClpP1 is much more active than MtClpP2 (discussed above). Fits of the data to this simple model are indicated by the solid lines in Fig. 4 *B* and *C*. With the exception of the activity profiles at the highest substrate values ([PKM-AMC] = 6 and 8 mM) and for very low [Bz-LL] in these cases, remarkably good fits are obtained considering that only two association constants, corresponding to Bz-LL and substrate binding to the *R* state of MtClpP1, are used. Monte Carlo simulations were used to estimate the uncertainties in the extracted parameters, and the distributions thus obtained for the free energies of substrate and Bz-LL binding and for the $T \rightleftharpoons R$ equilibrium are indicated in Fig. 4*F* for the simple model used. As mentioned above, the quality of the fits can be further improved by introducing binding to the second ring. We have found that a more complex model allowing for substrate and activator binding to the *R* states of MtClpP1 and MtClpP2 but where binding does not occur to the *T* states of the rings (i.e., only the right half of the binding model of Fig. 4*D* is operational) improves the quality of the activity fits for the high substrate concentrations used.

A number of important conclusions emerge from the fits that are not dependent on the chosen model. First, the data can only be fit with large *L* values ($\sim 2 \times 10^5$), reflecting that in the absence of Bz-LL the compact and functionally inactive *T*-state form of MtClpP1P2 is highly populated (~99.999% for the case of $L = 2 \times 10^5$). Second, binding of Bz-LL shifts the $T \rightleftharpoons R$ equilibrium to the active, extended *R* state, implying a higher Bz-LL affinity for the *R* state and resulting in the observed sigmoidal NMR intensity and activity profiles. Third, at high Bz-LL concentrations, the activity decreases, despite the increase in the population of *R*-state conformers, due to competitive inhibition between Bz-LL and substrate. The green profiles in Fig. 4 *B* and *C* show the average total number of bound Bz-LL molecules in the *R* state of MtClpP1 during the Bz-LL titration either without (Fig. 4*B*) or as a function of different concentrations of PKM-AMC (Fig. 4*C*), again assuming the simplest "single"-ring binding model. Notably, the number of bound Bz-LL molecules at maximum activity decreases with increasing PKM-AMC concentration, reflecting the competition between Bz-LL and substrate for the same binding sites as described above. Fourth, given that the MtClpP2 ring has little activity toward the PKM-AMC substrate (*SI Appendix*, Fig. S7) and that at maximum activity an MtClpP1 ring is bound with approximately four Bz-LL molecules (Fig. 4*C*, green line), most of the measured activity must derive from two or three unoccupied *R*-state MtClpP1 protomers. Finally, the significant decrease in enzyme activity at higher substrate concentrations provides strong evidence for substrate inhibition in this system (described below).

Allosteric Activation Is Both Intra- and Interring. As described above and illustrated in Fig. 3*E*, the activity response profile for MtClpP1P2 both increases and shifts to lower Bz-LL concentrations on binding of ADEP. As ADEP only binds to MtClpP2 (48, 49) (Fig. 3*A*), while the measured activity derives from MtClpP1, these assays suggest that the adjacent rings of a complex are able to communicate with each other. There is strong evidence that allostery between rings extends to individual subunits within a ring as well. For example, fitted parameters from MWC models that consider binding of Bz-LL to the *R* states of both MtClpP1 and MtClpP2 rings of the complex establish that Bz-LL binds with at least 10-fold higher affinity to MtClpP1. Activation of MtClpP1P2 originates, therefore, predominantly from Bz-LL binding to the MtClpP1 ring with propagation from nonfunctional Bz-LL–containing protomers to functional empty neighboring subunits within the active MtClpP1 ring. To provide further evidence of intraring communication, we have generated covalent complexes with the Z-Gly-Leu-Phe-chloromethyl ketone (GLF-CMK) mimic of substrate peptides that functions as an active site inhibitor because of its covalent attachment to the MtClpP1 ring of MtClpP1P2. Intact protein electrospray ionization mass spectrometry (ESI-MS) confirms that this inhibitor selectively modifies the MtClpP1 ring of the complex (*SI Appendix*, Fig. S9), with no reactivity toward MtClpP2. As a first step, the structure of the MtClpP1P2 complex with the MtClpP1 ring fully reacted with GLF-CMK was determined using cryo-EM (*SI Appendix*, Fig. S3*E*). After 2D and three-dimensional (3D) classification (*SI Appendix*, Fig. S3*F*), 143,748 particle images were used in a final refinement with C7 symmetry enforced, producing a 3D map at a resolution of 3.5 Å (*SI Appendix*, Fig. S4 *E* and *F*). An atomic model built into the cryo-EM map shows that MtClpP1P2 is in the extended conformation with a barrel height of 87 Å (Fig. 5*A*). Clear density for the GLF-CMK active site inhibitor in each of the seven active sites of the MtClpP1 ring (Fig. 5*B*) is consistent with intact protein mass spectrometry (*SI Appendix*, Fig. S9). Similar to the Bz-LL–bound conformation, the handle region has a well-defined structure (Fig. 5*C*), and the oligomerization switch is engaged (Fig. 5*D*). However, unlike the Bz-LL–bound form, density is not observed for the N-terminal domains of the protomers of the MtClpP2 ring in this fully modified MtClpP1P2 complex, suggesting that they are dynamic (Fig. 5*B* and *SI Appendix*, Fig. S10).

To evaluate how covalent modification of the MtClpP1 ring impacts the activity of the MtClpP1P2 complex that will provide evidence of intraring allostery, a series of protein samples where the MtClpP1 ring was partially modified by GLF-CMK was prepared by varying the ClpP:GLF-CMK ratio. The fraction of active sites modified (FM), defined as $FM = A_{Mod}/(A_{Mod} + A_{Unmod})$ where A_{Mod} and A_{Unmod} are the areas under the modified and unmodified ESI-MS protein peaks, respectively, was used to quantify the progress of the reaction (*SI Appendix*, Fig. S9). Samples ranging from no to full MtClpP1 modification were assayed for activity in the absence (Fig. 5*E*, white bars) and in the presence of Bz-LL (Fig. 5*E*, orange bars) using PKM-AMC as substrate. In the absence of GLF-CMK modification and without the addition of Bz-LL, the MtClpP1P2 complex is inactive, consistent with the assays in Fig. 1*B*. Notably, MtClpP1P2 is activated at an FM of 0.28 without the addition of Bz-LL, with maximum activity achieved at FM ~ 0.50, corresponding to modification of 3.5 of 7 MtClpP1 protomers on average. Thus, covalent modification of several catalytic S98 residues in the MtClpP1 ring leads to allosteric activation of the remaining protomers and generates a catalytically active enzyme. Further modification of the MtClpP1 ring reduces activity, and as expected, complete modification abolishes catalysis. Interestingly, the addition of Bz-LL to these mixtures consistently results in further activation. In the presence of Bz-LL, maximum activity is observed when the MtClpP1P2 complex is not modified and decreases at

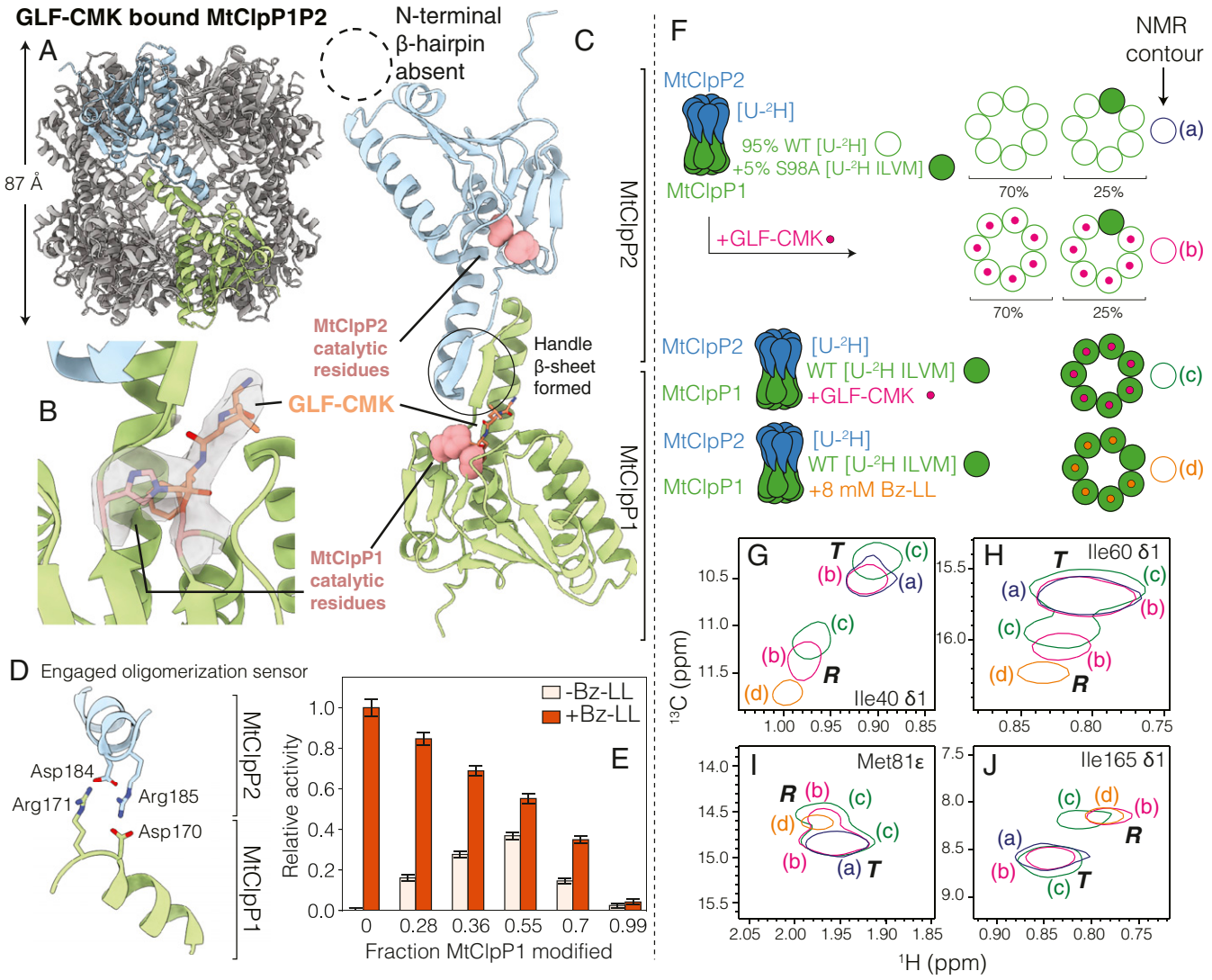

Fig. 5. Active site inhibitors activate MtClpP1P2 via intraring allosteric communication. (*A*) Side view of the cryo-EM structure of MtClpP1P2 where the active sites of MtClpP1 are fully modified by GLF-CMK. The height of the MtClpP1P2 complex (excluding the N-terminal β-hairpins of MtClpP2) is noted. (*B*) Close-up view of the catalytic His and Ser of an MtClpP1 protomer and cryo-EM density for the attached GLF-CMK (both His-123 and Ser-98 of the active site are covalently linked to the inhibitor). (*C*) Close-up view of a pair of opposite MtClpP1 (green) and MtClpP2 (blue) protomers showing an ordered handle β-sheet (solid circle) as a result of the modification of MtClpP1 by GLF-CMK. Notably, the N-terminal region of MtClpP2 (dotted circle) remains disordered. (*D*) Status of the oligomerization sensor of MtClpP1P2 in the GLF-CMK–modified form. Side chains of residues involved in salt bridge formation are indicated. (*E*) Activity of MtClpP1P2 complexes unmodified and partially modified with GLF-CMK assayed with 250 μM PKM-AMC substrate in the absence (white) and presence (orange; 8 mM) of Bz-LL (40 °C). The extent of the modification of the MtClpP1 ring of the MtClpP1P2 complex by GLF-CMK measured from intact protein mass spectrometry (*SI Appendix*, Fig. S9) is noted on the horizontal axis. Error bars correspond to 1 SD from the average of three replicates. (*F*) Cartoons of MtClpP1P2 complexes with spectra that are subsequently shown in *G–J*, indicating the labeling schemes used, and bound ligands. Complexes were generated where either all MtClpP1 protomers were WT or hybrid, with rings produced by mixing 95% [U-^{2}H] WT (open green circles; each circle corresponds to an MtClpP1 protomer) and 5% ILVM-labeled S98A protomers (filled green circles). In the latter case, MtClpP1 heptamers with distributions of WT and S98A subunits were produced, with the dominant configurations shown. These complexes were either subsequently reacted with the GLF-CMK active site inhibitor (pink circles) or not reacted; note that only WT protomers can react. Complexes were also obtained with all WT MtClpP1 protomers either GLF-CMK reacted (pink) or partially Bz-LL bound (8 mM; orange circles; with approximately six Bz-LL molecules bound to MtClpP1 at 8 mM as indicated). The color schematic for *G–J* is displayed. (*G–J*) Isolated regions of ^{1}H-^{13}C HMQC spectra (40 °C, 18.8 T) of selected residues from ILVM-labeled MtClpP1 in MtClpP1P2 complexes (WT ^{2}H-labeled MtClpP2). Subspectra of different complexes are shown as discussed in *F*. Correlations from *R* and *T* states are indicated along with resonance assignments for each panel. Spectra are displayed as single contours to avoid cluttering.

higher levels of MtClpP1 modification with the concomitant reduction in the number of active sites.

The presence of intraring allostery can be further demonstrated by NMR studies of hybrid MtClpP1 rings produced by mixing 95% [U-^{2}H] WT and 5% ILVM-labeled S98A protomers (Fig. 5*F*). The choice of a 95 to 5% ratio maximizes the probability of generating rings with NMR-active protomers surrounded by GLF-CMK–modified protomers (described below) so that the extent of intraprotomer communication within a ring can be assessed conclusively. The mixed rings are generated by unfolding WT and S98A protomers separately in guanidinium chloride followed by mixing of the two chain types and then, subsequent refolding to generate complexes whose composition and population that can be predicted using combinatorial statistics as shown in Fig. 5*F* and described previously (63, 64). These composite MtClpP1 heptamers were then mixed with a twofold excess of WT [U-^{2}H] MtClpP2 heptamers, and the complex reacted with GLF-CMK to modify all of the functionally active NMR-invisible WT MtClpP1

subunits (Fig. 5*F*, red dots). In contrast, NMR-visible S98A protomers do not react with GLF-CMK because they lack the catalytic serine; these ILVM protomers serve as NMR reporters of whether intraring (within an MtClpP1 ring) allostery is present. A second unreacted complex prepared in an otherwise identical fashion to the sample described above and a third complex that includes IVLM-labeled WT MtClpP1 and [U-^{2}H] WT MtClpP2, with the MtClpP1 fully reacted with GLF-CMK, were generated (Fig. 5*F*). Finally, a fourth complex mixed with 8 mM Bz-LL was produced (Fig. 5). Spectra of fully GLF-CMK–modified MtClpP1 within the MtClpP1P2 complex showed pairs of peaks for many residues (green single contours in Fig. 5 *G*–*J*), with one set of peaks at positions similar to those for the unreacted WT molecule (blue contours in Fig. 5 *G*–*J*) and a second set of correlations that overlap well with those from the Bz-LL–bound form of WT MtClpP1P2 (orange contours in Fig. 5 *G*–*J*). A similar set of pairs of peaks was observed for the mixed sample (NMR-invisible MtClpP2 + MtClpP1 composed of largely NMR-invisible GLF-CMK protomers doped with NMR-visible MtClpP1 protomers) (red single contours in in Fig. 5 *G*–*J*). These pairs of peaks report on an allosteric mechanism by which GLF-CMK binding to the active site of a protomer is transmitted to a second unbound subunit of the ring as the NMR active protomers are not GLF-CMK labeled. The NMR data (Fig. 5 *F*–*J*) and the activity assays of Fig. 5*E* can be explained in the context of our proposed MWC model in which the covalent attachment of GLF-CMK partially shifts the $T \rightleftharpoons R$ equilibrium toward the *R* state in a similar manner to Bz-LL binding, although in the latter case, the population can be completely shifted to the *R* conformation (Fig. 3*B*).

Discussion

M. tuberculosis takes advantage of a tightly regulated Clp protein degradation system that helps maintain cellular homeostasis and allows the pathogen to remain dormant in the host for decades (27, 28, 44). It comprises a protease component (ClpP) that collaborates with ATP-dependent unfoldases, ClpX or ClpC1, to recognize, unfold, translocate, and ultimately, destroy substrate proteins in the cell. The Clp system is essential for *M. tuberculosis* growth and virulence (26, 27), and as such, its disruption by small-molecule modulators with antibiotic activity has generated considerable attention (29–32, 65, 66). ClpPs from actinobacteria, such as MtClpP1P2 studied in this work, are unique in that they are catalytically dead on their own in vitro but can be activated by the presence of a number of dipeptides, such as Bz-LL used here (32, 36, 49, 53). The structural basis for their lack of activity and their activation mechanism have remained poorly characterized but require a detailed understanding for the rational design and improvement of pharmaceuticals, such as those used to target MtClpP1P2. Quantifying the structure–function–dynamics paradigm of MtClpP1P2 forms the basis of our present study.

An intriguing feature of ClpP proteases is their structural plasticity and allosteric properties. It has been shown that ClpP, while maintaining its tetradecameric architecture, can assume several conformations that mainly differ in the height of its barrel-like structure and in the conformation of the handle domain (11, 67). High-resolution ClpP structures from various species include an active extended conformation with a fully formed catalytic triad and handle domain (38, 68) as well as compressed/compact forms with kinked/truncated handle helices and unstructured handle β-sheets with misaligned active site residues (69–72). While it is widely accepted that the extended form is prevalent in solution and is the active state, it has yet to be established whether the compressed/compact forms can be populated under conditions that are distinct from those used for crystallization, where crystal contacts can affect the ClpP structure (11, 73).

Our study provides an important first step toward the goal of manipulating MtClpP1P2 function by providing the structural basis for why this complex is catalytically dead in the absence of activator peptides and why, unlike for many other ClpPs, binding of ADEPs does not activate the protein. The 3.0-Å resolution structure from cryo-EM of the apo form of MtClpP1P2 shows that the complex is in the compact conformation. The hallmarks of the compact form are truncated handle helices and disordered handle β-strands that lead to an impaired catalytic triad, thereby explaining the lack of activity observed for the apo state of the complex. Notably, while ADEP binding to MtClpP1P2 leads to an ordering of the N-terminal region of MtClpP2, the handle region remains disordered so that the active site residues are not properly positioned with respect to each other for catalysis. The binding of ADEP, as described here, as well as either ClpA or ClpC1 to MtClpP1P2 (28, 53) results in a significant shift in the MtClpP1P2 activity response curve to lower Bz-LL concentrations, suggesting that the concomitant use of active site inhibitors together with ADEP might increase the susceptibility of *M. tuberculosis* to antibiotic treatment. A common problem with active site inhibitors, such as Bortezomib, that are successful in inhibiting MtClpP1P2 activity and consequently, the growth of *M. tuberculosis* (36) is that they lack specificity and lead to unwanted modification of serine proteases and the host proteasome (35). However, a recent study has shown that replacement of the boronate moiety of Bortezomib with chloromethyl ketone results in specificity toward MtClpP1P2, acceptable cytotoxicity against *M. tuberculosis*, and no activity toward the human proteasome (34), suggesting that it may be possible to engineer therapeutics that target specifically the MtClpP1P2 enzyme. Our results, showing a disordered handle region in the absence of activators, provide a possible starting point for the rational development of specific inhibitors that focus on regions of the structure distinct from the active site that are unique to MtClpP1P2. Notably, novel noncovalent inhibitors have been designed to exploit the dynamic nature of the handle helix to actuate a conformational change in the handle domain that distorts the catalytic triad in *S. aureus* ClpP (19).

The pervasive contributions of allostery in the MtClpP1P2 system are highlighted by our study. The binding of ADEP exclusively to sites in MtClpP2 leads to enhanced catalytic activity of active sites in MtClpP1 that is only possible via interring communication. Addition of the active site inhibitor GLF-CMK to generate a fraction of MtClpP1 protomers that are modified at catalytic serine residues resulted in activation of an otherwise catalytically dead enzyme, suggesting an important role for intraprotomer communication within a single ring. The high degree of allostery has been captured by a modified MWC model that reproduces how activator peptide Bz-LL binding to MtClpP1P2 leads to the conversion from a catalytically dead *T* state to an active *R* conformation, as observed through large chemical shift perturbations in NMR titration spectra, and accounts for the activity vs. Bz-LL concentration profiles as a function of PKM-AMC substrate concentration. The functional assays show a marked decrease in activity with increasing substrate concentration past a certain threshold that can be accounted for by invoking substrate inhibition and taken into account in our MWC model (*SI Appendix*). A model of substrate rather than product inhibition is more likely for a number of reasons. First, substrate degradation kinetics were linear over the complete time course examined, while product inhibition would lead to decreased rates over time. Second, activity profiles decreased with increasing substrate concentration beyond PKM-AMC substrate concentrations of ∼1 mM, despite the fact that the amount of product produced also decreased. It is estimated that in ∼20% of enzymes the substrate may serve as an inhibitor (74), controlling enzyme activity during periods of unusually low or high metabolic activity. Substrate activation and inhibition might be advantageous for an organism like *M. tuberculosis* with a slow growth rate that must retain viability during latent infections (75). Down-regulation of MtClpP1P2 activity in response to extreme substrate concentrations, either low or high, could reduce spurious degradation of small disordered proteins or newly

synthesized polypeptides, which have yet to fold properly, that diffuse into the degradation chamber independent of regulatory unfoldases.

Although our model accounts for all of the measured experimental data, at least when substrate and activator binding to both rings of the complex is considered (*SI Appendix*, Fig. S8), we have not been able to cross-validate the presence of an independent site that binds substrate and leads to inhibition. Titration of substrate into a sample with active MtClpP1P2 results in rapid hydrolysis. Generation of a catalytically dead enzyme by substituting active site Ser residues in MtClpP1 and MtClpP2 with Ala circumvents this problem but generates enzymes with properties that are different from those of the WT. For example, the *T* to *R* transition occurs at Bz-LL concentrations that are fivefold reduced for the Ser to Ala mutant, and a complex that is composed of WT MtClpP1 and S110A MtClpP2 has an activity profile that is different from the WT enzyme with a shift in activity to lower Bz-LL concentrations.

Although binding of active site inhibitors has been reported to activate *L. monocytogenes* ClpP (76) and the β-subunits of the proteasome with trypsin-like activities (77), a mechanistic understanding of this phenomenon has been lacking. Previous studies made use of a multipronged approach involving isothermal calorimetry, NMR spectroscopy, crystallography, and functional assays to understand the mechanism of allosteric activation of *Thermus thermophilus* ClpP (TtClpP) (78). It was shown that nonsaturating concentrations of the active site inhibitor Bortezomib lead to an activation that is moderately cooperative, with an activity profile that could be fit with a Hill coefficient of 1.3. Notably, Bortezomib binding resulted in opening of the N-terminal axial pores that enabled the passage and degradation of larger substrates by TtClpP. The structural differences between the conformers involved in the allosteric transition could not be established experimentally, however, as both the apo and the Bortezomib-bound forms crystalized in the extended conformation. However, the authors used molecular dynamics simulations to conclude that the less active form is likely the compressed state of the complex, with kinked handle helices.

The allosteric model of ClpP activation based on an equilibrium between active and inactive conformations is useful to understand why some ClpPs, such as those from *T. thermophilus* and *M. tuberculosis*, exhibit non-Michaelis Menten kinetics and cooperative activation and why others, such as *E. coli* ClpP, have unusually high substrate proteolysis rates with no requirement for activator peptides (36). In the framework of the MWC model, the equilibrium between *T* and *R* states would be shifted much more closely to *R* for ClpP from *E. coli* than for TtClpP, which in turn, is significantly closer to *R* than is the case for MtClpP1P2. Our modeling of Bz-LL binding data and activity profiles suggests that 0.0005% of the MtClpP1P2 molecules in solution are in a catalytically competent state in the absence of activator. By contrast, ∼25% of TtClpP molecules are in an active state. The unusually high population of *T* conformers for MtClpP1P2 relative to other ClpPs suggests that, if the *T* state could be targeted perhaps through the distorted handle region, it may be possible to achieve a degree of specificity toward the *M. tuberculosis* enzyme.

The extent of allostery likely represents an important layer of regulation of ClpP activity that is carefully tuned in each organism. In the case of dormant bacterial populations of *M. tuberculosis*, cellular homeostasis would require a tight regulation of all components of the protein degradation machinery so that spurious substrate removal is limited (13, 14). This regulation is partly achieved through the binding of ClpC1 or ClpX regulatory particles, which control substrate entry, in addition to affecting ClpP protease activity (28, 44). A second layer of protection against unwanted degradation is afforded by the modest affinities of MtClpP1 and MtClpP2 for each other and the fact that individual ClpP rings are catalytically dead since interactions between Asp and Arg residues on adjacent rings are required to couple the oligomerization state of the enzyme to its catalytic activity. Finally, a third layer of control is provided by allostery, allowing MtClpP1P2 to adjust its activity in response to high concentrations of substrates. In this way, the enzyme remains inactive, even in a tetradecameric form, unless a certain activating threshold of substrate is achieved. For Bz-LL and GLF-CMK, it seems that, on average, binding of roughly four molecules is needed for optimal activity. Although high concentrations of Bz-LL activator are required for the conversion to the catalytic state, it is worth noting that the presence of a single translocated substrate trapped in the catalytic chamber of MtClpP1P2 with an internal volume of 65,600 $Å^3$ (79) corresponds to an effective concentration of ∼25 mM that could be sufficient to promote activity. Thus, the activation mechanism described here may also occur in vivo, where both the binding of AAA+ unfoldases and the translocation of substrates bearing activating sequences lead to the stabilization of the extended form of MtClpP1P2 so that efficient and processive substrate degradation is enabled.

Materials and Methods

Details of protein expression and purification and biochemical and biophysical measurements along with data fitting and derivation of analytical models are provided in *SI Appendix*.

ACKNOWLEDGMENTS. We thank Dr. Samir Benlekbir for assistance with cryo-EM data collection on the Titan Krios; Prof. Walid A. Houry (University of Toronto) for the gift of ADEP; Prof. Eric J. Rubin (Harvard University), Dr. Tatos Akopian (Harvard University), and Dr. Olga Kandror (Harvard University) for an initial supply of Bz-LL and for valuable discussions; Dr. Algirdas Velyvis (University of Toronto), Dr. Jacob P. Brady (University of Toronto), Dr. Justin M. Di Trani (University of Toronto), Sina Ghiassian (University of Alberta), and Banafsheh Rafiee (University of Alberta) for help with data fitting and error analysis; and Dr. Robert Vernon (Hospital for Sick Children) for valuable discussions and assistance with Rosetta modeling. S.V. and Z.A.R. were supported by a postdoctoral fellowship and a scholarship, respectively, from the Canadian Institutes of Health Research. J.L.R. and L.E.K. were supported by the Canada Research Chairs program. This research was funded by Canadian Institutes of Health Research Grants PJT-162186 (to J.L.R) and MOP-133408 (to L.E.K). Titan Krios cryo-EM data were collected at the Toronto High-Resolution High-Throughput cryo-EM facility supported by the Canadian Foundation for Innovation and the Ontario Research Fund.

1. J. Furin, H. Cox, M. Pai, Tuberculosis. *Lancet* **393**, 1642–1656 (2019).
2. WHO, Global Tuberculosis Report 2019. https://www.who.int/tb/publications/global_report/en/. Accessed 11 November 2019.
3. C.-C. Shu, K.-M. Liao, Y.-C. Chen, J.-J. Wang, C.-H. Ho, The burdens of tuberculosis on patients with malignancy: Incidence, mortality and relapse. *Sci. Rep.* **9**, 11901 (2019).
4. J. Bruchfeld, M. Correia-Neves, G. Källenius, Tuberculosis and HIV coinfection. *Cold Spring Harb. Perspect. Med.* **5**, a017871 (2015).
5. S. H. Gillespie, Evolution of drug resistance in Mycobacterium tuberculosis: Clinical and molecular perspective. *Antimicrob. Agents Chemother.* **46**, 267–274 (2002).
6. V. Ramappa, G. P. Aithal, Hepatotoxicity related to anti-tuberculosis drugs: Mechanisms and management. *J. Clin. Exp. Hepatol.* **3**, 37–49 (2013).
7. W. W. Yew, C. C. Leung, Antituberculosis drugs and hepatotoxicity. *Respirology* **11**, 699–707 (2006).
8. R. van Hest *et al.*, Hepatotoxicity of rifampin-pyrazinamide and isoniazid preventive therapy and tuberculosis treatment. *Clin. Infect. Dis.* **39**, 488–496 (2004).
9. M. A. Behr, P. H. Edelstein, L. Ramakrishnan, Revisiting the timetable of tuberculosis. *BMJ* **362**, k2738 (2018).
10. R. M. G. J. Houben, P. J. Dodd, The global burden of latent tuberculosis infection: A re-estimation using mathematical modelling. *PLoS Med.* **13**, e1002152 (2016).
11. K. Liu, A. Ologbenla, W. A. Houry, Dynamics of the ClpP serine protease: A model for self-compartmentalized proteases. *Crit. Rev. Biochem. Mol. Biol.* **49**, 400–412 (2014).
12. V. Bhandari *et al.*, The role of ClpP protease in bacterial pathogenesis and human diseases. *ACS Chem. Biol.* **13**, 1413–1425 (2018).
13. A. O. Olivares, T. A. Baker, R. T. Sauer, Mechanistic insights into bacterial AAA+ proteases and protein-remodelling machines. *Nat. Rev. Microbiol.* **14**, 33–44 (2016).
14. A. L. Goldberg, Protein degradation and protection against misfolded or damaged proteins. *Nature* **426**, 895–899 (2003).
15. D. Frees, U. Gerth, H. Ingmer, Clp chaperones and proteases are central in stress survival, virulence and antibiotic resistance of *Staphylococcus aureus*. *Int. J. Med. Microbiol.* **304**, 142–149 (2014).

16. C. M. Pickart, R. E. Cohen, Proteasomes and their kin: Proteases in the machine age. *Nat. Rev. Mol. Cell Biol.* **5**, 177–187 (2004).
17. F. Ye, J. Li, C. G. Yang, The development of small-molecule modulators for ClpP protease activity. *Mol. Biosyst.* **13**, 23–31 (2016).
18. T. Böttcher, S. A. Sieber, β-lactones as privileged structures for the active-site labeling of versatile bacterial enzyme classes. *Angew. Chem. Int. Ed. Engl.* **47**, 4600–4603 (2008).
19. M. W. Hackl *et al*., Phenyl esters are potent inhibitors of caseinolytic protease P and reveal a stereogenic switch for deoligomerization. *J. Am. Chem. Soc.* **137**, 8475–8483 (2015).
20. M. Lakemeyer *et al*., Tailored peptide phenyl esters block ClpXP proteolysis by an unusual breakdown into a heptamer-hexamer assembly. *Angew. Chem. Int. Ed. Engl.* **58**, 7127–7132 (2019).
21. C. Moreno-Cinos *et al*., ClpP protease, a promising antimicrobial target. *Int. J. Mol. Sci.* **20**, 2232 (2019).
22. J. Kirstein *et al*., The antibiotic ADEP reprogrammes ClpP, switching it from a regulated to an uncontrolled protease. *EMBO Mol. Med.* **1**, 37–49 (2009).
23. M. Gersch *et al*., AAA+ chaperones and acyldepsipeptides activate the ClpP protease via conformational control. *Nat. Commun.* **6**, 6320 (2015).
24. K. S. Wong *et al*., Acyldepsipeptide analogs dysregulate human mitochondrial ClpP protease activity and cause apoptotic cell death. *Cell Chem. Biol.* **25**, 1017–1030.e9 (2018).
25. K. Gerdes, H. Ingmer, Antibiotics: Killing the survivors. *Nature* **503**, 347–349 (2013).
26. C. M. Sassetti, D. H. Boyd, E. J. Rubin, Genes required for mycobacterial growth defined by high density mutagenesis. *Mol. Microbiol.* **48**, 77–84 (2003).
27. R. M. Raju *et al*., Mycobacterium tuberculosis ClpP1 and ClpP2 function together in protein degradation and are required for viability in vitro and during infection. *PLoS Pathog.* **8**, e1002511 (2012).
28. K. R. Schmitz, R. T. Sauer, Substrate delivery by the AAA+ ClpX and ClpC1 unfoldases activates the mycobacterial ClpP1P2 peptidase. *Mol. Microbiol.* **93**, 617–628 (2014).
29. E. Gavrish *et al*., Lassomycin, a ribosomally synthesized cyclic peptide, kills mycobacterium tuberculosis by targeting the ATP-dependent protease ClpC1P1P2. *Chem. Biol.* **21**, 509–518 (2014).
30. W. Gao *et al*., The cyclic peptide ecumicin targeting ClpC1 is active against Mycobacterium tuberculosis in vivo. *Antimicrob. Agents Chemother.* **59**, 880–889 (2015).
31. M. P. Choules *et al*., Rufomycin targets ClpC1 proteolysis in Mycobacterium tuberculosis and M. Abscessus. *Antimicrob. Agents Chemother.* **63**, e02204-18 (2019).
32. K. Famulla *et al*., Acyldepsipeptide antibiotics kill mycobacteria by preventing the physiological functions of the ClpP1P2 protease. *Mol. Microbiol.* **101**, 194–209 (2016).
33. T. Akopian *et al*., The active ClpP protease from M. tuberculosis is a complex composed of a heptameric ClpP1 and a ClpP2 ring. *EMBO J.* **31**, 1529–1541 (2012).
34. W. Moreira, S. Santhanakrishnan, B. W. Dymock, T. Dick, Bortezomib warhead-switch confers dual activity against mycobacterial caseinolytic protease and proteasome and selectivity against human proteasome. *Front. Microbiol.* **8**, 746 (2017).
35. W. Moreira *et al*., Towards selective mycobacterial ClpP1P2 inhibitors with reduced activity against the human proteasome. *Antimicrob. Agents Chemother.* **61**, e02307-16 (2017).
36. T. Akopian *et al*., Cleavage specificity of Mycobacterium tuberculosis ClpP1P2 protease and identification of novel peptide substrates and boronate inhibitors with anti-bacterial activity. *J. Biol. Chem.* **290**, 11008–11020 (2015).
37. Y. Yang *et al*., Inhibiting Mycobacterium tuberculosis ClpP1P2 by addressing the equatorial handle domain of ClpP1 subunit. bioRxiv:10.1101/713214 (24 July 2019).
38. J. Wang, J. A. Hartling, J. M. Flanagan, The structure of ClpP at 2.3 A resolution suggests a model for ATP-dependent proteolysis. *Cell* **91**, 447–456 (1997).
39. S. R. Geiger, T. Böttcher, S. A. Sieber, P. Cramer, A conformational switch underlies ClpP protease function. *Angew. Chem. Int. Ed. Engl.* **50**, 5749–5752 (2011).
40. M. C. Bewley, V. Graziano, K. Griffin, J. M. Flanagan, Turned on for degradation: ATPase-independent degradation by ClpP. *J. Struct. Biol.* **165**, 118–125 (2009).
41. A. Szyk, M. R. Maurizi, Crystal structure at 1.9A of E. coli ClpP with a peptide covalently bound at the active site. *J. Struct. Biol.* **156**, 165–174 (2006).
42. Y. Katayama *et al*., The two-component, ATP-dependent Clp protease of Escherichia coli. Purification, cloning, and mutational analysis of the ATP-binding component. *J. Biol. Chem.* **263**, 15226–15236 (1988).
43. T. A. Baker, R. T. Sauer, ClpXP, an ATP-powered unfolding and protein-degradation machine. *Biochim. Biophys. Acta* **1823**, 15–28 (2012).
44. A. A. H. Alhuwaider, D. A. Dougan, AAA+ machines of protein destruction in mycobacteria. *Front. Mol. Biosci.* **4**, 49 (2017).
45. Y. Personne, A. C. Brown, D. L. Schuessler, T. Parish, Mycobacterium tuberculosis ClpP proteases are co-transcribed but exhibit different substrate specificities. *PLoS One* **8**, e60228 (2013).
46. H. Ingvarsson *et al*., Insights into the inter-ring plasticity of caseinolytic proteases from the X-ray structure of Mycobacterium tuberculosis ClpP1. *Acta Crystallogr. D Biol. Crystallogr.* **63**, 249–259 (2007).
47. N. Benaroudj, B. Raynal, M. Miot, M. Ortiz-Lombardia, Assembly and proteolytic processing of mycobacterial ClpP1 and ClpP2. *BMC Biochem.* **12**, 61 (2011).
48. J. Leodolter, J. Warweg, E. Weber-Ban, The Mycobacterium tuberculosis ClpP1P2 protease interacts asymmetrically with its ATPase partners ClpX and ClpC1. *PLoS One* **10**, e0125345 (2015).
49. K. R. Schmitz, D. W. Carney, J. K. Sello, R. T. Sauer, Crystal structure of Mycobacterium tuberculosis ClpP1P2 suggests a model for peptidase activation by AAA+ partner binding and substrate delivery. *Proc. Natl. Acad. Sci. U.S.A.* **111**, E4587–E4595 (2014).
50. E. Zeiler *et al*., Structural and functional insights into caseinolytic proteases reveal an unprecedented regulation principle of their catalytic triad. *Proc. Natl. Acad. Sci. U.S.A.* **110**, 11302–11307 (2013).
51. M. Dahmen, M.-T. Vielberg, M. Groll, S. A. Sieber, Structure and mechanism of the caseinolytic protease ClpP1/2 heterocomplex from Listeria monocytogenes. *Angew. Chem. Int. Ed. Engl.* **54**, 3598–3602 (2015).
52. S. Pan, I. T. Malik, D. Thomy, B. Henrichfreise, P. Sass, The functional ClpXP protease of Chlamydia trachomatis requires distinct clpP genes from separate genetic loci. *Sci. Rep.* **9**, 14129 (2019).
53. M. Li *et al*., Structure and functional properties of the active form of the proteolytic complex, ClpP1P2, from Mycobacterium tuberculosis. *J. Biol. Chem.* **291**, 7465–7476 (2016).
54. V. Tugarinov, P. M. Hwang, J. E. Ollerenshaw, L. E. Kay, Cross-correlated relaxation enhanced 1H[bond]13C NMR spectroscopy of methyl groups in very high molecular weight proteins and protein complexes. *J. Am. Chem. Soc.* **125**, 10420–10428 (2003).
55. R. Rosenzweig, L. E. Kay, Bringing dynamic molecular machines into focus by methyl-TROSY NMR. *Annu. Rev. Biochem.* **83**, 291–315 (2014).
56. S. Schütz, R. Sprangers, Methyl TROSY spectroscopy: A versatile NMR approach to study challenging biological systems. *Prog. Nucl. Magn. Reson. Spectrosc.*, 10.1016/j.pnmrs.2019.09.004 (2019).
57. R. Sprangers, A. Velyvis, L. E. Kay, Solution NMR of supramolecular complexes: Providing new insights into function. *Nat. Methods* **4**, 697–703 (2007).
58. J. Wang, J. A. Hartling, J. M. Flanagan, Crystal structure determination of Escherichia coli ClpP starting from an EM-derived mask. *J. Struct. Biol.* **124**, 151–163 (1998).
59. A. Gribun *et al*., The ClpP double ring tetradecameric protease exhibits plastic ring-ring interactions, and the N termini of its subunits form flexible loops that are essential for ClpXP and ClpAP complex formation. *J. Biol. Chem.* **280**, 16185–16196 (2005).
60. M. Gersch, A. List, M. Groll, S. A. Sieber, Insights into structural network responsible for oligomerization and activity of bacterial virulence regulator caseinolytic protease P (ClpP) protein. *J. Biol. Chem.* **287**, 9484–9494 (2012).
61. T. L. Religa, R. Sprangers, L. E. Kay, Dynamic regulation of archaeal proteasome gate opening as studied by TROSY NMR. *Science* **328**, 98–102 (2010).
62. J. Monod, J. Wyman, J.-P. Changeux, On the nature of allosteric transitions: A plausible model. *J. Mol. Biol.* **12**, 88–118 (1965).
63. R. Huang, F. Pérez, L. E. Kay, Probing the cooperativity of *Thermoplasma acidophilum* proteasome core particle gating by NMR spectroscopy. *Proc. Natl. Acad. Sci. U.S.A.* **114**, E9846–E9854 (2017).
64. S. Vahidi *et al*., Reversible inhibition of the ClpP protease via an N-terminal conformational switch. *Proc. Natl. Acad. Sci. U.S.A.* **115**, E6447–E6456 (2018).
65. K. Weinhäupl *et al*., The antibiotic cyclomarin blocks arginine-phosphate-induced millisecond dynamics in the N-terminal domain of ClpC1 from *Mycobacterium tuberculosis*. *J. Biol. Chem.* **293**, 8379–8393 (2018).
66. R. M. Raju, A. L. Goldberg, E. J. Rubin, Bacterial proteolytic complexes as therapeutic targets. *Nat. Rev. Drug Discov.* **11**, 777–789 (2012).
67. M. Stahl, S. A. Sieber, An amino acid domino effect orchestrates ClpP's conformational states. *Curr. Opin. Chem. Biol.* **40**, 102–110 (2017).
68. J. Ishizawa *et al*., Mitochondrial ClpP-mediated proteolysis induces selective cancer cell lethality. *Cancer Cell* **35**, 721–737.e9 (2019).
69. M. S. Kimber *et al*., Structural and theoretical studies indicate that the cylindrical protease ClpP samples extended and compact conformations. *Structure* **18**, 798–808 (2010).
70. F. Ye *et al*., Helix unfolding/refolding characterizes the functional dynamics of *Staphylococcus aureus* Clp protease. *J. Biol. Chem.* **288**, 17643–17653 (2013).
71. B.-G. Lee, M. K. Kim, H. K. Song, Structural insights into the conformational diversity of ClpP from Bacillus subtilis. *Mol. Cells* **32**, 589–595 (2011).
72. L. Díaz-Sáez, G. Pankov, W. N. Hunter, Open and compressed conformations of Francisella tularensis ClpP. *Proteins* **85**, 188–194 (2017).
73. J. A. Alexopoulos, A. Guarné, J. Ortega, ClpP: A structurally dynamic protease regulated by AAA+ proteins. *J. Struct. Biol.* **179**, 202–210 (2012).
74. M. C. Reed, A. Lieb, H. F. Nijhout, The biological significance of substrate inhibition: A mechanism with diverse functions. *BioEssays* **32**, 422–429 (2010).
75. H. Getahun, A. Matteelli, R. E. Chaisson, M. Raviglione, Latent Mycobacterium tuberculosis infection. *N. Engl. J. Med.* **372**, 2127–2135 (2015).
76. D. Balogh *et al*., Insights into ClpXP proteolysis: Heterooligomerization and partial deactivation enhance chaperone affinity and substrate turnover in *Listeria monocytogenes*. *Chem. Sci. (Camb.)* **8**, 1592–1600 (2017).
77. M. Groll, C. R. Berkers, H. L. Ploegh, H. Ovaa, Crystal structure of the boronic acid-based proteasome inhibitor bortezomib in complex with the yeast 20S proteasome. *Structure* **14**, 451–456 (2006).
78. J. Felix *et al*., Mechanism of the allosteric activation of the ClpP protease machinery by substrates and active-site inhibitors. *Sci. Adv.* **5**, eaaw3818 (2019).
79. M. F. Mabanglo *et al*., ClpP protease activation results from the reorganization of the electrostatic interaction networks at the entrance pores. *Commun. Biol.* **2**, 410 (2019).